Trachyandesitic volcanism in the early Solar System

Addi Bischoff[a,1], Marian Horstmann[a], Jean-Alix Barrat[b], Marc Chaussidon[c], Andreas Pack[d], Daniel Herwartz[d,e], Dustin Ward[a], Christian Vollmer[f], and Stephan Decker[g]

[a]Institut für Planetologie and [f]Institut für Mineralogie, Westfälische Wilhelms-Universität Münster, 48149 Münster, Germany; [b]Institut Universitaire Européen de la Mer, Université de Bretagne Occidentale, 29280 Plouzané, France; [c]Institut de Physique du Globe, 75235 Paris, France; [d]Geowissenschaftliches Zentrum, Universität Göttingen, 37077 Göttingen, Germany; [e]Institut für Geologie und Mineralogie, Universität zu Köln, 50674 Köln, Germany; and [g]Meteorite Museum, 55430 Oberwesel, Germany

Edited by Mark H. Thiemens, University of California, San Diego, La Jolla, CA, and approved July 23, 2014 (received for review March 13, 2014)

Volcanism is a substantial process during crustal growth on planetary bodies and well documented to have occurred in the early Solar System from the recognition of numerous basaltic meteorites. Considering the ureilite parent body (UPB), the compositions of magmas that formed a potential UPB crust and were complementary to the ultramafic ureilite mantle rocks are poorly constrained. Among the Almahata Sitta meteorites, a unique trachyandesite lava (with an oxygen isotope composition identical to that of common ureilites) documents the presence of volatile- and SiO_2-rich magmas on the UPB. The magma was extracted at low degrees of disequilibrium partial melting of the UPB mantle. This trachyandesite extends the range of known ancient volcanic, crust-forming rocks and documents that volcanic rocks, similar in composition to trachyandesites on Earth, also formed on small planetary bodies ∼4.56 billion years ago. It also extends the volcanic activity on the UPB by ∼1 million years (Ma) and thus constrains the time of disruption of the body to later than 6.5 Ma after the formation of Ca–Al-rich inclusions.

differentiation | meteorite parent body | achondrites | differentiated meteorites

A large number of planetary embryos, tens to hundreds of kilometers in size, accreted within the early Solar System. In some of these embryos, internal heating triggered melting and differentiation, giving rise to a varied suite of lithologies as documented by the achondritic meteorites. Planetary crustal growth occurs via both volcanic eruptions and plutonic intrusions. Constraining these processes and the diversity of crustal materials that formed the outermost solid shell of planetary bodies is crucial for understanding Solar System planetary processes and evolution.

Ureilites are among the most common achondrites and represent remnants of the mantle from a planetary body from which magmas have been extensively extracted (1–4). Several details of ureilite petrogenesis (e.g., the mode of melt extraction) remain controversial (e.g., refs. 1 and 2) because crustal rocks from the ureilite parent body (UPB) have not yet been discovered. Although tiny remnants of feldspathic and felsic melts from ureilitic breccias have been interpreted as UPB basalts or products of partial melting of plagioclase-bearing cumulates (e.g., refs. 5 and 6), it is generally assumed that the complementary melts were lost to space during explosive eruptions (e.g., refs. 7–9).

A unique opportunity to gain new insights into ureilite petrogenesis was provided by the polymict asteroid 2008 TC_3 that impacted our planet October 7, 2008, in the Nubian Desert, Sudan, containing various ureilitic and ureilite-related fragments (10, 11). Among its remnant fragments collected in the strewn field, collectively named the "Almahata Sitta" meteorites, the sample ALM-A (Almahata Sitta trachyandesitic meteorite) was recovered (12). ALM-A weights 24.2 g and is covered with a greenish and shiny fusion crust (Fig. 1).

The ALM-A sample described here is the only SiO_2-rich, rapidly cooled volcanic rock among the meteorites in our collections. This rock is texturally completely different from the felsic achondrite Graves Nunatak (GRA) 06128/9 (13) and granitic lithologies that occur as fragments in meteorite breccias (14). GRA 06128/9 shows a plutonic, granoblastic texture, 120° triple junctions between coexisting phases, and chemically equilibrated silicates (13). ALM-A clearly demonstrates that SiO_2-rich lavas were formed on the UPB and sets new important constraints on ureilite petrogenesis.

Results

The oxygen isotope compositions of two ALM-A aliquots (Fig. 2) were constrained to $\delta^{18}O = 8.1$ ‰, $\delta^{17}O = 3.2$ ‰, $\Delta^{17}O = -1.06$ ‰ and $\delta^{18}O = 8.0$ ‰, $\delta^{17}O = 3.2$ ‰, $\Delta^{17}O = -1.04$ ‰ (for details, see *SI Appendix*). They fall in the range of other ureilites, including those from Almahata Sitta (10, 11, 15, 16), but at the ^{16}O-poor end of the range of oxygen isotopes in ureilites, which is the more common oxygen isotope composition found among ureilites.

ALM-A (Fig. 1; see *SI Appendix*, Tables S1– S3 and Figs. S1–S3 for mineralogical details and the compositions of the constituent phases) is a fine-grained rock rich in feldspars (∼70 vol%; subhedral, zoned plagioclase with $\sim An_{10-55}$ and anhedral anorthoclase with $\sim An_{5-12}$) embedding abundant Cr-bearing (Cr_2O_3: ∼0.8–1 wt%) Ca pyroxene (∼20 vol %; $\sim Fs_{19-25}Wo_{34-41}$) having glass inclusions, and low-Ca pyroxene (∼5 vol%; $\sim Fs_{32-42}Wo_{8-14}$) without any exsolution lamellae. Anorthoclase was identified by Raman spectroscopy (*SI Appendix*, Fig. S4). As accessory phases, euhedral Cl apatite (with ∼0.3 wt% H_2O), merrillite, ilmenite, Ti,Cr,Fe-spinel, FeS, and Ni-poor Fe metal (Ni <0.10 wt%) are observed (Fig. 1). Fine-grained intergrowths of albitic feldspar ($An_{<10}$), skeletal pyroxene, and a K_2O-rich, quartz-normative glass (with up to ∼4.5 wt% K_2O and up to ∼40 μm in size) are found in interstices between the major minerals. These glasses are rhyolitic in composition, indicating the possibility for formation of rocks with even higher SiO_2 concentrations on the UPB (granitoids or granites; compare ref. 17). Considering the

Significance

Volcanism is a fundamental geological process on planets and was substantial during crustal growth on planetary bodies in the early Solar System, as witnessed by ubiquitous rocks of basaltic composition, e.g., on Earth, Moon, Mars, and asteroids. Besides basaltic volcanism, trachyandesite lavas are generated on Earth. The first occurrence of a trachyandesite lava in the meteorite collections demonstrates that trachyandesitic, alkali-, and silica-rich volcanism takes place not only on Earth today but already occurred on a small planetesimal ∼4.56 billion years ago. It sets new constraints on mechanisms and styles of early Solar System volcanism.

Author contributions: A.B. designed research; A.B., M.H., J.-A.B., M.C., A.P., D.H., D.W., and C.V. performed research; A.B., M.H., J.-A.B., M.C., A.P., D.H., D.W., and C.V. analyzed data; A.B., M.H., J.-A.B., M.C., A.P., D.H., D.W., C.V., and S.D. wrote the paper; and S.D. identified the sample.

The authors declare no conflict of interest.

This article is a PNAS Direct Submission.

[1]To whom correspondence should be addressed. Email: bischoa@uni-muenster.de.

This article contains supporting information online at www.pnas.org/lookup/suppl/doi:10.1073/pnas.1404799111/-/DCSupplemental.

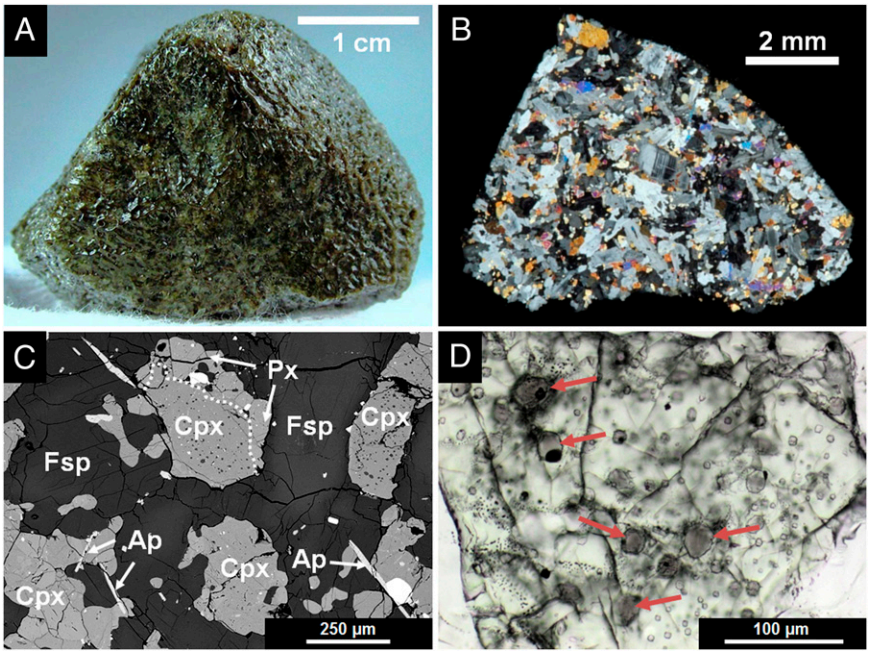

Fig. 1. (*A*) Greenish ALM-A hand specimen, (*B*) overview of the ALM-A thin section (polarized light, crossed nicols) showing high abundances of feldspar (mainly gray) and displaying a subdoleritic texture. Anhedral anorthoclase and subhedral, zoned plagioclase laths occur. Low-Ca and Ca pyroxene (both colored) are frequently encountered. (*C*) Close-up backscattered electron image illustrating the textural relation of feldspar (Fsp) and pyroxenes (Cpx, Ca rich; Px, low Ca). Ca pyroxene bears abundant inclusions of, e.g., feldspar and SiO_2-rich glass. Cl apatite (Ap) is developed as laths. (*D*) Quartz-normative, alkali-rich glass inclusions occur within large Ca pyroxene crystals (arrows; polarized light).

studied thin sections, the ALM-A rock is free of vesicles and olivine phenocrysts.

ALM-A has a trachyandesitic bulk chemical composition. Trachyandesite is a lava, rich in feldspars and containing—depending on the concentrations of $Na_2O + K_2O$—between 53 wt% SiO_2 and 63 wt% SiO_2 using the International Union of Geological Sciences criteria. ALM-A has high concentrations of alkalis (~7 wt% of $Na_2O + K_2O$), about 60 wt% SiO_2, and is Mg rich (MgO = 4.8 wt%; Table 1). The composition results in a Mg number (mg#) [=100×Mg/(Mg+Fe)] close to 61, which is similar to, e.g., those of some terrestrial primitive basalts or Mg-rich andesites. ALM-A displays enrichments of Ba, Be, Th, U, Nb, Ta, Eu, Ti, Zr, Hf, and Sr relative to the light rare earth elements (REE) [e.g., $(Th/La)_n$ = 1.64, Eu/Eu*= 1.63, $(Sr/Ce)_n$ = 1.79, $(Hf/Sm)_n$ = 1.70], and a significant heavy REE enrichment [$(Gd/Lu)_n$ = 0.78] (Fig. 3*A* and *SI Appendix*, Fig. S5).

^{26}Al-^{26}Mg systematics of seven feldspar grains indicate that ALM-A crystallized 6.5 (+0.5, −0.3) million years (Ma) after Ca–Al-rich inclusions (CAIs) (Fig. 4 and *SI Appendix*, Table S4 and Fig. S6) and is thus ~1 Ma younger than the monomict Northwest Africa (NWA) 766 ureilite (18) and the albitic clasts found in polymict ureilites (19).

Discussion

Although ALM-A is unlike all previously described achondrites, there is clear evidence that the rock originated from the ureilite parent body: (*i*) The oxygen isotope composition of ALM-A (Fig. 2) falls in the field of the ureilites and feldspathic clasts from polymict ureilites (3, 20, 21); (*ii*) the feldspar mineralogy is very similar to the rare feldspathic clasts found in some polymict ureilites, which are considered as remnants of UPB melts (5); and (*iii*) it is most likely part of asteroid 2008 TC_3, which was shown to be a fragment of an asteroid dominated by ureilitic lithologies (10, 11).

The presence of glass (*SI Appendix*, Fig. S3) and anorthoclase (*SI Appendix*, Fig. S4), a phase occasionally occurring in terrestrial lava bombs, indicates very rapid cooling of ALM-A (22, 23), in accordance with a lava origin on the UPB.

Contrary to terrestrial trachyandesites, which are generally residual melts formed from more mafic magmas by fractional

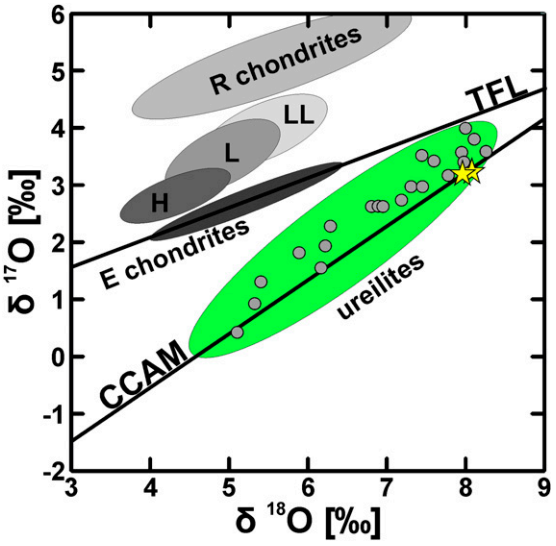

Fig. 2. Three-oxygen isotope diagram illustrating the bulk composition (two aliquots) of ALM-A (yellow stars) in comparison with ureilite data from Almahata Sitta ureilites (gray dots). The oxygen isotope compositions of two ALM-A aliquots are compared with data on other ureilitic samples from Almahata Sitta (10, 11, 15, 16). Green field highlights the compositional range for oxygen isotope compositions of other ureilites (20). Gray fields give the compositional ranges for Rumuruti (R) chondrites, ordinary chondrites (H, L, LL), and enstatite (E) chondrites. TFL, terrestrial fractionation line; CCAM, carbonaceous chondrite–anhydrous mineral line.

Table 1. Major and trace element abundances in the ALM-A meteorite

Oxides	ALM-A	Elements	ALM-A	Elements	ALM-A	Elements	ALM-A
SiO_2	60.07	Li	3.95	Nb	2.57	Ho	0.467
TiO_2	0.67	Be	0.23	Mo	0.017	Er	1.40
Al_2O_3	14.66	Sc	21.4	Cs	1.11	Tm	0.221
Cr_2O_3	0.28	V	26.1	Ba	22.06	Yb	1.50
FeO	5.57	Co	1.55	La	1.44	Lu	0.224
MnO	0.27	Ni	7.33	Ce	3.54	Hf	1.22
MgO	4.81	Cu	1.44	Pr	0.546	Ta	0.133
CaO	7.29	Zn	148	Nd	2.92	W	0.011
Na_2O	6.59	Ga	30.2	Sm	1.01	Pb	0.15
K_2O	0.29	Rb	4.57	Eu	0.628	Th	0.284
P_2O_5	0.52	Sr	85.8	Gd	1.46	U	0.078
Total	101.02	Y	12.63	Tb	0.280		
		Zr	38.27	Dy	1.96		

Oxides in wt%; other elements in micrograms per gram.

crystallization, ALM-A was certainly not affected substantially by this process. It has been observed that the $\Delta^{17}O$ of ureilites correlates with the FeO in their olivines (*SI Appendix*, Fig. S7). Assuming that $\Delta^{17}O$ does not change during partial melting, ALM-A's source rock (i.e., the UPB mantle) had olivine compositions of $Fo_{78–86}$. Using an olivine/melt distribution coefficient $K_D(Fe/Mg)$ $[=(Fe/Mg)_{olivine}/(Fe/Mg)_{melt}]$ of 0.28 (24), the conjugate melts in equilibrium with such sources have mg# numbers in the range 50–63. ALM-A's mg# value is 61 and is well in this range and supports an origin from the UPB.

The compositions of the first melts produced during equilibrium melting of typical chondrites at low pressure are controlled by the enstatite–plagioclase–forsterite peritectic in the olivine–plagioclase–silica system and would be basaltic in composition (25). Intermediate melts were suggested by gabbroic, plagioclase-, and diopside-rich inclusions in the Caddo County iron meteorite (26) and the felsic achondrite GRA 06128/9 (13), but the inferred

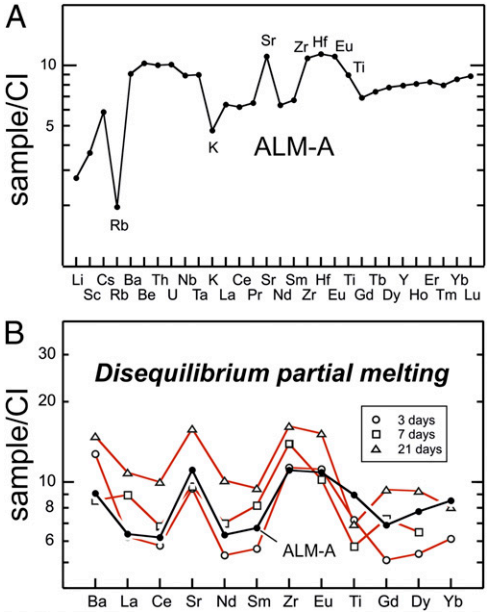

Fig. 3. (*A*) Bulk trace element pattern of ALM-A (200-mg aliquot) and (*B*) selected trace elements of ALM-A (black line) compared with those of the experimental melts produced by disequilibrium melting of an ordinary chondrite [Leedey, L6, red lines (29)] normalized to CI chondrite values (33).

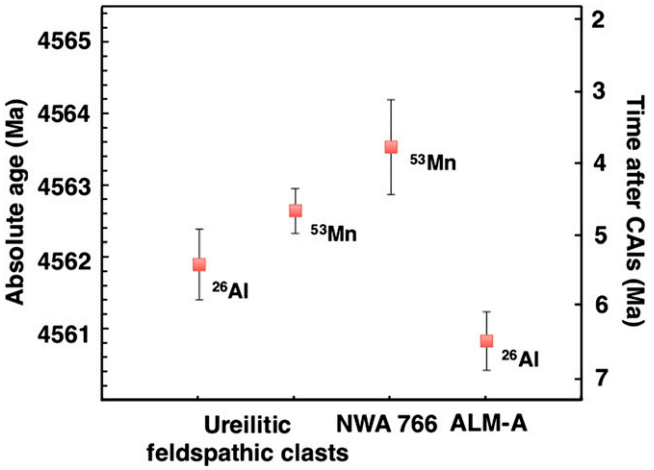

Fig. 4. Al-Mg age of ALM-A compared with Al-Mg and Mn-Cr ages obtained from albitic clasts found in polymict ureilites (19) considering (34) and the Mn-Cr age of the NWA 766 ureilite (18).

compositions of their parental melts are still a matter of debate (e.g., ref. 27). If the melted lithologies are more silica rich, as exemplified by the FeO-poor enstatite chondrites or other pyroxene-rich source rocks, the compositions of the melts are controlled by the enstatite–plagioclase–silica peritectic. Although such melts are more silica- and plagioclase-rich and have andesitic or trachyandesitic compositions (28), they will be much poorer in FeO than ALM-A. Therefore, an origin of ALM-A from an enstatite chondrite-like parent body is excluded.

The CI1-normalized element abundances in ALM-A show some anomalies. The concentrations of Sr, Eu, Zr, Hf, and Ti are slightly higher than expected for equilibrium partial melting of a source rock of chondritic composition, whereas concentrations of Rb and K are lower (*SI Appendix*, Fig. S8). Experimental data on disequilibrium partial melt compositions (51–56 wt% SiO_2, up to 4.4 wt% Na_2O) of an ordinary chondrite starting material [10–15% melting (29)], however, are close to the observed silica- and Na-rich composition of ALM-A, and well match the observed Sr, Eu, Zr, and Ti concentrations (Fig. 3). It cannot be completely ruled out that the Sr, Ba, and Eu concentrations may result from volatility-related processes during the experiments and are not an effect of the rapidity of melting. In any case, ALM-A's trace element features (Fig. 3) must be genuine characteristics of the melt. Recent experimental works have demonstrated that low-degree melting (<5%) of an oxidized chondrite (R chondrite) even better matches the bulk compositions of ALM-A [and GRA 06128/9 (30)], in terms of major element chemistry (~61 wt% SiO_2, ~9 wt% Na_2O). Generation of ALM-A by disequilibrium melting of chondritic source rock suggests that the ALM-A melt was rapidly extracted. Rapid melt extraction was also considered in previous models of magma genesis on the UPB (1, 31).

The abundances of volatiles (F, Cl, and OH) displayed by ALM-A's apatites (*SI Appendix*, Table S3) indicate that these elements were involved during the melting on the UPB, and have certainly favored the segregation of the melts from their sources and their transport to the surface.

The discovery of ALM-A shows that a crust with an intermediate composition on the UPB was at least partially preserved and that the lavas were not entirely lost to space by explosive volcanism as generally assumed (e.g., refs. 7–9). Beyond that, ALM-A is ~1 Ma younger than the albitic clasts found in polymict ureilites [5.5 Ma after CAIs (18)], extending the igneous activity on the ureilite parent body for at least another 1 Ma. Although the duration of the entire magmatic activity of

the UPB cannot be directly estimated, the thermal history of the ureilites indicates that their parent body was impact-disrupted while still hot [~1200–1300 °C (32)]. These temperatures are in the range of temperatures required to produce melts on the UPB. This implies that magmatic activity was still ongoing on the UPB at the time, when the planetesimal was destroyed by a giant collision. The age of the catastrophic event is not known, but ALM-A constrains the time of disruption to ≥ 6.5 Ma after the formation of CAIs.

The unique ALM-A trachyandesite demonstrates that silica-rich magmas were generated on small planetary bodies early in Solar System history.

Methods

For mineralogical characterization, the sample was studied by optical and electron microscopy. A JEOL 6610-LV electron microscope (SEM) was used to resolve the fine-grained textures, and quantitative mineral analyses were obtained using a JEOL JXA 8900 Superprobe electron microprobe (EPMA) operated at 15 keV and a probe current of 15 nA at the Westfälische Wilhelms-Universität Münster. For the bulk chemical analysis, a 200-mg chip was powdered. An aliquot of 115 mg was used for the determination of trace elements by inductively coupled plasma (ICP)-MS, and with the remaining material the major elements were determined by ICP-atomic emission spectroscopy. The oxygen isotope compositions of two aliquots of ALM-A were measured by laser fluorination gas mass spectrometry (see *SI Appendix* for details). At the CRPG-CNRS (Nancy) the Mg isotopic compositions and Al/Mg concentration ratios were measured with the Cameca IMS 1280-HR2 ion microprobe. Raman spectroscopy was performed at the Institut für Mineralogie of the Westfälische Wilhelms-Universität Münster. The spectra of selected areas within grains of interest were acquired on a Horiba Scientific XploRA confocal Raman microscope. Details on the procedures and standards are given in *SI Appendix*.

ACKNOWLEDGMENTS. We thank Moritz Barth for assistance, Herbert Kroll for comments and discussions on the anorthoclase mineralogy, and R. C. Maury for discussions on andesites and adakites. Jasper Berndt and Beate Schmitte are acknowledged for assistance with EPMA work. We very much appreciate the very constructive and helpful comments of the reviewers Hilary Downes and Paul Warren and the editor Mark H. Thiemens for handling the manuscript. This study was partly supported by the German Research Foundation within the Priority Program "The First 10 Million Years of the Solar System—A Materials Approach" (SPP 1385) and by the Programme National de Planetologie de l'Institut National des Sciences de L'Univers.

1. Goodrich CA, Van Orman J, Wilson L (2007) Fractional melting and smelting on the ureilite parent body. *Geochim Cosmochim Acta* 71(11):2876–2895.
2. Warren PH (2012) Parent body depth–pressure–temperature relationships and the style of the ureilite anatexis. *Meteorit Planet Sci* 47:209–227.
3. Downes H, Mittlefehldt DW, Kita NT, Valley JW (2008) Evidence from polymict ureilite meteorites for a disrupted and re-accreted single ureilite parent asteroid gardened by several distinct impactors. *Geochim Cosmochim Acta* 72(19):4825–4844.
4. Mittlefehldt DW, McCoy TJ, Goodrich CA, Kracher A Non-chondritic meteorites from asteroidal bodies. *Planetary Materials*, ed Papike JJ, Reviews in Mineralogy (Mineral Soc of Am, Washington), Vol 26, pp 4-1–4-195.
5. Cohen BA, Goodrich CA, Keil K (2004) Feldspathic clast populations in polymict ureilites: Stalking the missing basalts from the ureilite parent body. *Geochim Cosmochim Acta* 68(20):4249–4266.
6. Ikeda Y, Prinz M, Nehru CE (2000) Lithic and mineral clasts in the Dar Al Gani (DAG) 319 polymict ureilite. *Antarct Meteorite Res* 13:177–221.
7. Warren PH, Kallemeyn GW (1992) Explosive volcanism and the graphite oxygen fugacity buffer on the parent asteroid(s) of the ureilite meteorites. *Icarus* 100:110–126.
8. Scott ERD, Taylor GJ, Keil K (1993) Origin of ureilite meteorites and implications for planetary accretion. *Geophys Res Lett* 20:415–418.
9. Wilson L, Keil K (2012) Volcanic activity on differentiated asteroids: A review and analysis. *Chem Erde* 72:289–321.
10. Jenniskens P, et al. (2009) The impact and recovery of asteroid 2008 TC_3. *Nature* 458(7237):485–488.
11. Bischoff A, Horstmann M, Pack A, Laubenstein M, Haberer S (2010) Asteroid 2008 TC_3 - Almahata Sitta: A spectacular breccia containing many different ureilitic and chondritic lithologies. *Meteorit Planet Sci* 45:1638–1656.
12. Bischoff A, Horstmann M, Pack A, Herwartz D, Decker S (2013) Almahata Sitta sample MS-MU-011: A rapidly crystallized basalt from the crust of the ureilite parent body. *Meteorit Planet Sci* 48:A60 (abstr).
13. Day JMD, et al. (2009) Early formation of evolved asteroidal crust. *Nature* 457(7226): 179–182.
14. Terada K, Bischoff A (2009) Asteroidal granite-like magmatism 4.53 Gyr ago. *Astrophys J* 699:L68–L71.
15. Rumble D, Zolensky ME, Friedrich JM, Jenniskens P, Shaddad MH (2010) The oxygen isotope composition of Almahata Sitta. *Meteorit Planet Sci* 45:1765–1770.
16. Horstmann M, et al. (2012) Mineralogy and oxygen isotope composition of new samples from the Almahata Sitta strewn field. *Meteorit Planet Sci* 47:A193.
17. Downes H, Beard AD, Howard K (2009) Petrology of a granitic clast in polymict ureilite EET87720. *Meteorit Planet Sci* 44:A63.
18. Yamakawa A, Yamashita K, Makishima A, Nakamura E (2010) Chromium isotope systematics of achondrites: Chronology and isotopic heterogeneity of the inner solar system bodies. *Astrophys J* 720:150–154.
19. Goodrich CA, et al. (2010) ^{53}Mn-^{53}Cr and ^{26}Al-^{26}Mg ages of a feldspathic lithology in polymict ureilites. *Earth Planet Sci Lett* 295:531–540.
20. Clayton RN, Mayeda TK (1996) Oxygen isotope studies of achondrites. *Geochim Cosmochim Acta* 60(11):1999–2017.
21. Kita NT, et al. (2004) Origin of ureilites inferred from a SIMS oxygen isotopic and trace element study of clasts in the Dar al Gani 319 polymict ureilite. *Geochim Cosmochim Acta* 68(20):4213–4235.
22. Dunbar NW, Cashman KV, Dupré R (1994) Crystallization processes of anorthoclase phenocrysts in the Mout Erebus magmatic system: Evidence from crystal composition, crystal size distributions, and volatile contents of melt inclusions. *Volcanological and Environmental Studies of Mount Erebus, Antarctica*, Antarct Res Ser, ed Kyle PR (AGU, Washington), Vol 66, pp 129–146.
23. Sims KWW, et al. (2013) On the time scales of magma genesis, melt evolution, crystal growth rates and magma degassing in the Erebus volcano magmatic system using the ^{238}U, ^{235}U and ^{232}Th decay series. *J Petrol* 54:235–271.
24. Kushiro I, Mysen BO (2002) A possible effect of melt structure on the Mg-Fe2+ partitioning between olivine and melt. *Geochim Cosmochim Acta* 66(12):2267–2272.
25. Stolper E (1977) Experimental petrology of eucritic meteorites. *Geochim Cosmochim Acta* 41(5):587–611.
26. Takeda H, Bogard DD, Mittlefehldt DW, Garrison DH (2000) Mineralogy, petrology, chemistry, and ^{39}Ar-^{40}Ar and exposure ages of the Caddo County IAB iron: Evidence for early partial melt segregation of a gabbro area rich in plagioclase-diopside. *Geochim Cosmochim Acta* 64(7):1311–1327.
27. Shearer CK, et al. (2010) Non-basaltic asteroidal melting during the earliest stages of solar system evolution. A view from Antarctic achondrites Graves Nunatak 06128 and 06129. *Geochim Cosmochim Acta* 74(3):1172–1199.
28. McCoy TJ, Dickinson TL, Lofgren GE (1999) Partial melting of the Indarch (EH4) meteorite: A textural, chemical, and phase relations view of melting and melt migration. *Meteorit Planet Sci* 34:735–746.
29. Feldstein SN, Jones RH, Papike JJ (2001) Disequilibrium partial melting experiments on the Leedey L6 chondrite: Textural controls on melting processes. *Meteorit Planet Sci* 36:1421–1441.
30. Gardner Vandy KG, et al. (2014) Making evolved melts on asteroids. *Lunar Planet Sci* 45:1483 (abstr).
31. Wilson L, Goodrich CA, Van Orman JA (2008) Thermal evolution and physics of melt extraction on the ureilite parent body. *Geochim Cosmochim Acta* 72(24):6154–6176.
32. Miyamoto M, Takeda H, Toyoda H (1985) Cooling history of some Antarctic ureilites. *J Geophys Res* 90(S01):116–122.
33. Barrat JA, et al. (2012) Geochemistry of CI chondrites: Major and trace elements, and Cu and Zn Isotopes. *Geochim Cosmochim Acta* 83:79–92.
34. Brennecka GA, Wadhwa M (2012) Uranium isotope compositions of the basaltic angrite meteorites and the chronological implications for the early Solar System. *Proc Natl Acad Sci USA* 109(24):9299–9303.

Supporting Information

S1 Text

Methods

Scanning electron microscopy and electron microprobe analysis

The mineralogy and texture of the ALM-A specimen were studied by optical and electron microscopy. A JEOL 6610-LV electron microscope (SEM) at the Interdisciplinary Center for Electron Microscopy and Microanalysis (ICEM) at the Westfälische Wilhelms-Universität Münster was used to resolve the fine-grained textures and for identification of the different mineral phases present. The EDS system attached (INCA; Oxford Instruments) was used for chemical characterization of the different mineral constituents at 20 keV. The beam current was controlled with a Faraday Cup. As natural and synthetic standards (Astimex) olivine (Mg, Fe, Si), jadeite (Na), plagioclase (Al), sanidine (K), diopside (Ca), rutile (Ti), chromium-oxide (Cr), rhodonite (Mn), and pentlandite (Ni) were used.

Quantitative mineral analyses were obtained using a JEOL JXA 8900 Superprobe electron microprobe (EPMA) at the ICEM operated at 15 keV and a probe current of 15 nA. Natural and synthetic standards were used for wavelength dispersive spectrometry. For feldspar analyses these were jadeite (Na), sanidine (K), diopside (Ca), anorthite (Si), plagioclase (Al), and fayalite (Fe). Counting times for feldspar analyses were 5s and 2.5s on the peak and background, respectively. Jadeite (Na), kyanite (Al), sanidine (K), chromium oxide (Cr), San Carlos olivine (Mg), hypersthene (Si), diopside (Ca), rhodonite (Mn), rutile (Ti), and fayalite (Fe) were used as standards when analyzing Ca- and low-Ca pyroxene, Fe,Ti,Cr-spinel, ilmenite, and SiO_2-rich material. Counting times for all elements were 10s peak and 5s background, except for Na and K with 5s peak and 2.5s background. The matrix corrections were made according to the $\Phi\rho(z)$ procedure (1).

Operating conditions during the analyses of the apatites were 15 keV accelerating voltage and a beam current of 10 nA with a defocussed beam of 5 µm. In order to cover possible ionic substitutions, 15 elements were measured using the subsequent standards: Astimex fluorite (Ca, F), Astimex apatite (P), USNM Rockport fayalite (Fe), USNM San Carlos olivine (Mg), rhodonite (Mn), celestine (Sr, S), jadeite (Na), sanidine (K), hypersthene (Si), Astimex rutile (Ti), kyanite (Al), Astimex chromium oxide (Cr) and Astimex tugtupite (Cl). Both of the halogens were measured first in the routine and exposed to a lower beam current of 5 nA to prevent migration or loss of volatiles. Counting times were 10s on peak and 5s on

background. The hydroxyl content was calculated by difference according to atomic proportions, assuming an occupation of the x-site with two anions and a total of $X_{Cl} + X_F + X_{OH} = 1$.

Bulk chemical analysis

A 200 mg chip was powdered using a boron carbide mortar and pestle. 115 mg of the powder were used for the determination of trace elements by ICP-MS, and the remaining powder was used for the determination of the major elements by ICP-AES. The procedures have been extensively described (2). Based on replicate standards, the precision for abundances and trace element ratios are better than 5 % (2 x relative standard deviation).

Oxygen isotope analysis

The oxygen isotope compositions of two aliquots of ALM-A were measured by laser fluorination gas mass spectrometry (3,4). Sample material (typically ~2-3 mg) is reacted with purified F_2 gas with aid of a 50 W infrared laser. Excess F_2 is reacted to Cl_2 in a NaCl trap (150°C) and Cl_2 is trapped in a liquid N_2 cold trap (-196°C). Sample O_2 is purified from trace gases (e.g. NF_3 and CF_4) using gas a chromatographic column and subsequently analyzed in dual inlet mode with a ThermoElectron MAT 253 gas mass spectrometer (4). Accuracy and precision in $\delta^{18}O$ and $\delta^{17}O$ are typically better than ±0.2 and ±0.1 ‰ (2 sigma), respectively (4). The $\Delta^{17}O$ (error: $\Delta^{17}O$ = ±0.02 ‰ (2 sigma)) is defined as $\Delta^{17}O = 1000*\ln(\delta^{17}O/1000+1)-0.5305*1000*\ln(\delta^{18}O/1000+1)$ (4,5).

Al-Mg analysis

The Mg isotopic compositions and Al/Mg concentration ratios were measured with the CRPG-CNRS Cameca ims 1280HR2 ion microprobe. Because of the low Mg contents of the feldspars, the measurements were made in mono-collection mode using the central electron multiplier (EM) for $^{24}Mg^+$, $^{25}Mg^+$ and $^{26}Mg^+$ and the central Faraday cup (FC2) for $^{27}Al^+$. The samples were sputtered with a ~20 nA O^- primary beam and the secondary ions analyzed at a mass resolution M/DM ~3500. One measurement was made of 75 cycles with counting times during each cycle of 4, 3, 10, 10, 3 and 3 sec at masses 23.8 (background for EM), ^{24}Mg, ^{25}Mg, ^{26}Mg, 26.8 (background FC2) and ^{27}Al, respectively. The Mg isotopic compositions are given in delta notation according to $\delta^{25}Mg_X=[(^{25}Mg/^{24}Mg)_X/(^{25}Mg/^{24}Mg)_{standard} - 1]\times1000$ (similarly for ^{26}Mg) with $(^{25}Mg/^{24}Mg)_{standard} = 0.12663$ and $(^{26}Mg/^{24}Mg)_{standard} = 0.13932$. The ^{26}Mg excesses are noted $\Delta^{26}Mg$ with $\Delta^{26}Mg = \delta\,^{26}Mg - \delta\,^{25}Mg/0.521$. Two in house synthetic

glasses of anorthitic composition (An#1 with $^{27}Al/^{24}Mg$=177.9 and An#2 with $^{27}Al/^{24}Mg$=19.4) and with no ^{26}Mg excess ($\Delta^{26}Mg$ = 0‰) were used to calibrate the instrumental isotopic fractionation law and the relative Al/Mg ion yield (6). Two sigma standard errors on the mean of ±0.26‰, ±0.37‰ and ±0.27‰ for $\delta^{25}Mg$, $\delta^{26}Mg$ and $\Delta^{26}Mg$, respectively, were obtained for 13 measurements of the standards. The relative Al/Mg ion yield was determined to be 0.985±0.021. The errors reported for the measurements of the samples are two sigma errors calculated by summing in quadratic way the errors due to counting statistic in each point and the error due to calibration of instrumental isotopic fractionation and Al/Mg ion yield.

Data for 7 different feldspar crystals are given in Table S4. Each data corresponds to the average of 2 to 4 replicate analyses in a given crystal within ~100 µm distance. The $^{27}Al/^{24}Mg$ ratios and $\Delta^{26}Mg$ values are quite constant for the 7 feldspars analyzed, ranging from 1076±9 to 1434±41 and from +0.45±1.04‰ to +1.38±0.66‰, respectively. A ^{26}Al isochron forced to $\Delta^{26}Mg$ =0±0.2‰ at $^{27}Al/^{24}Mg$ = 0 was calculated through these points. This gives a $^{26}Al/^{27}Al$ ratio of 1.1×10^{-7} ($\pm0.4\times10^{-7}$) corresponding to an age difference of 6.5 Ma (+0.5, -0.3Ma) relative to the $^{26}Al/^{27}Al$ ratio determined from the bulk CAI isochron ($^{26}Al/^{27}Al$ =5.23×10^{-5}; (7)).

Micro-Raman Spectroscopy

Raman spectra of selected areas within grains of interest were acquired on a Horiba Scientific XploRA^{TM} confocal Raman microscope of the Institut für Mineralogie at the Westfälische Wilhelms-Universität Münster. The green laser (532 nm, 5-6 mW) and an entrance slit of 100 µm resulted in an energy resolution of a few wave numbers sufficient for fingerprinting. The standard hole of 500 µm was chosen for a penetration depth of ~1 µm, spatial resolution with these laser and spectrometer settings was also around this value. Calibration of the system was checked before analysis on a silicon standard using the first order Raman band of 520.7 cm^{-1}. The 100× objective lens of the microscope was used for spectrum collection, measurement time per spot was 60 or 120 seconds. Raman bands were dispersed by a grating of 2400 grooves per mm giving a wave number range from 100 to 1100 cm^{-1} on a Peltier-cooled CCD camera.

1. Armstrong JT (1991) Quantitative elemental analysis of individual microparticles with electron beam instruments. *In Electron Probe Quantitation,* eds Heinrich KFJ, Newbury DE, Plenum Press, New York, 261-315.

2. Barrat JA, et al. (2012) Geochemistry of CI chondrites: Major and trace elements, and Cu and Zn Isotopes. *Geochim Cosmochim Acta* 83:79-92.

3. Sharp ZD (1990) A laser-based microanalytical technique for *in situ* determination of oxygen isotope ratios of silicates and oxides, *Geochim Cosmochim Acta* 54:1353-1357.

4. Pack A, Herwartz D (2014) The triple oxygen isotope composition of the Earth mantle and understanding $\Delta^{17}O$ variations in terrestrial rocks and minerals. *Earth Planet Sci Lett* 390:138-145.

5. Miller MF (2002) Isotopic fractionation and the quantification of ^{17}O anomalies in the oxygen three-isotope system: an appraisal and geochemical significance, *Geochim Cosmochim Acta* 66:1881-1889.

6. Luu T-H, et al. (2013) High precision Mg isotope measurements of meteoritic samples by secondary ion mass spectrometry. *J Anal. At. Spectrom.* 28, 67-76.

7. Jacobsen B, et al. (2008) ^{26}Al-^{26}Mg and ^{207}Pb-^{206}Pb systematics of Allende CAIs: Canonical solar initial $^{26}Al/^{27}Al$ ratio reinstated. *Earth Planet Sci Lett* 272:353–364.

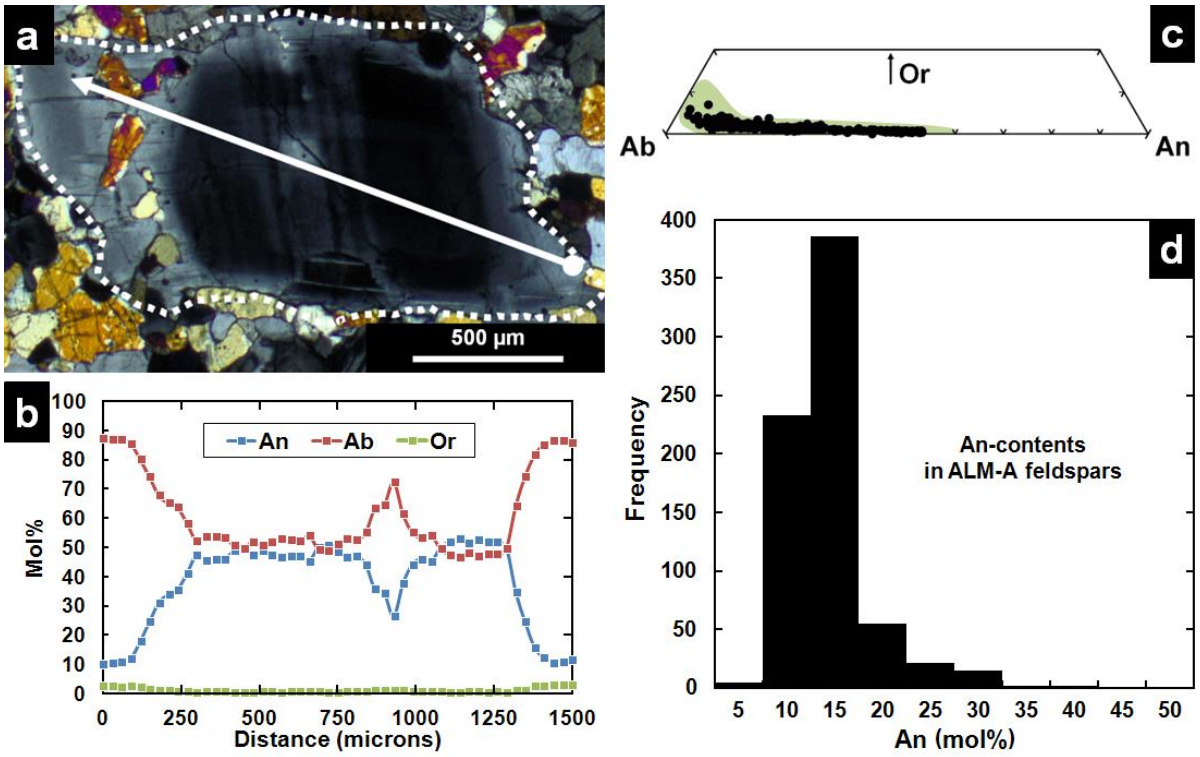

Fig. S1. a) Photomicrograph in polarized light (crossed nicols) of a chemically zoned ALM-A feldspar across which the zoning profile illustrated in b) was taken [anorthite (An)-, albite (Ab)-, and orthoclase (Or)-contents given in mol%]. White arrow in a) points the direction of the profile. No other grain with such a complicated zoning profile has been observed. c) Compositional range of feldspar in ALM-A. Green field denotes the feldspar compositions in feldspathic fragments from polymict ureilites (1). d) Frequency distribution of An compositions in ALM-A feldspars. A total of 720 analyses were performed in grid mode by SEM. Feldspar compositions peak at ~An_{10-15}, while more calcic compositions (up to ~An_{55}) are much less abundant and occur in some crystal cores (compare (a)).

1. Cohen BA, Goodrich CA, Keil K (2004) Feldspathic clast populations in polymict ureilites: Stalking the missing basalts from the ureilite parent body. *Geochim Cosmochim Acta* 68:4249-4266.

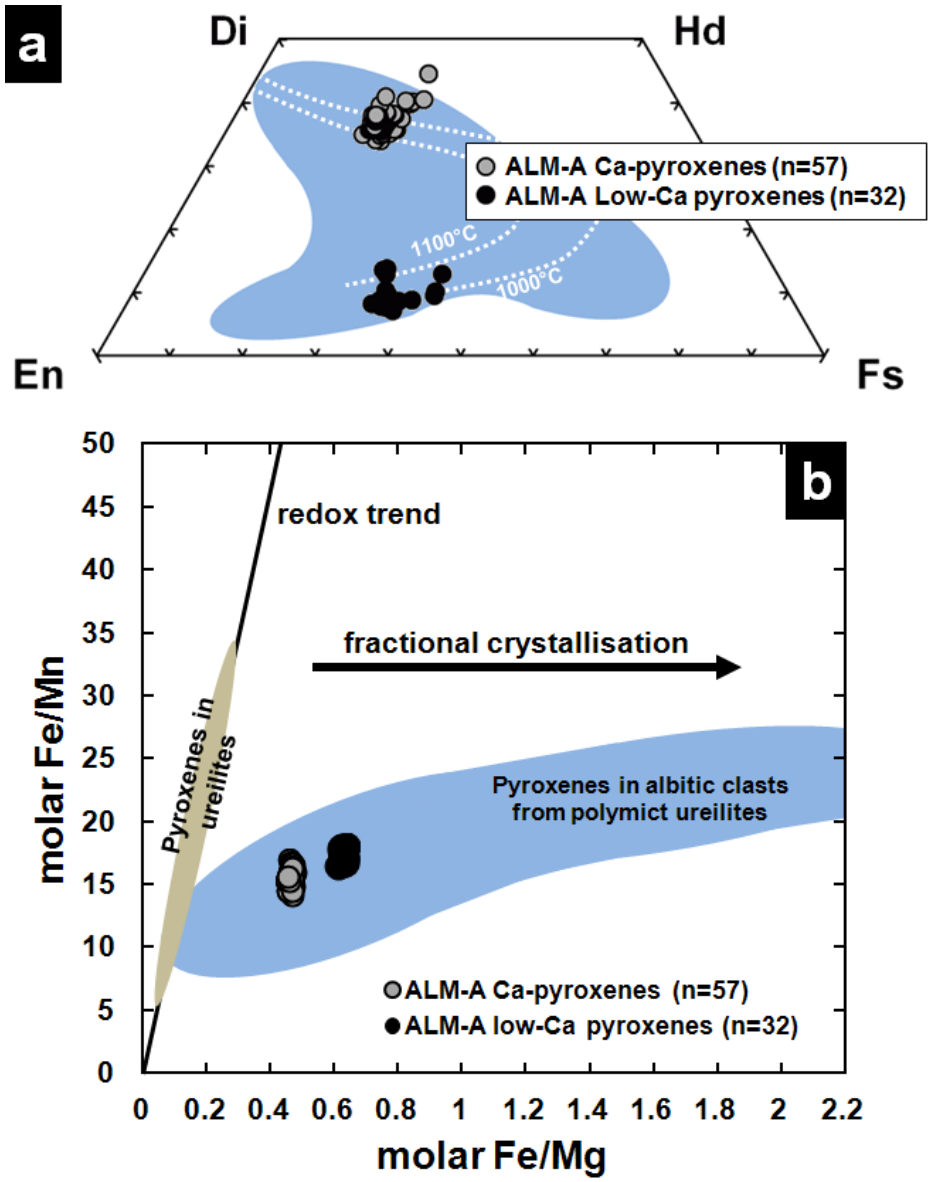

Fig. S2. a) Chemical compositions low-Ca and Ca-pyroxene in ALM-A compared with the range of pyroxene compositions in albitic fragments from polymict ureilites (blue, Cohen et al., (1)). Shown as white dashed lines are isotherms at 1 bar from Lindsley (2). b) Molar Fe/Mg vs. Fe/Mn in ALM-A pyroxenes compared with data for pyroxenes in feldspathic clasts from polymict ureilites. Shown for comparison are literature data (1,3) for pyroxene in ureilites (khaki) and within the albitic clasts from polymict ureilites (grey). Figure b) after Goodrich et al. (3).

1. Cohen BA, Goodrich CA, Keil K (2004) Feldspathic clast populations in polymict ureilites: Stalking the missing basalts from the ureilite parent body. *Geochim Cosmochim Acta* 68:4249-4266.

2. Lindsley DH (1983) Pyroxene thermometry. *Am Mineral* 68:477-493.

3. Goodrich CA, et al. (2010) ^{53}Mn-^{53}Cr and ^{26}Al-^{26}Mg ages of a feldspathic lithology in polymict ureilites. *Earth Planet Sci Lett* 295:531-540.

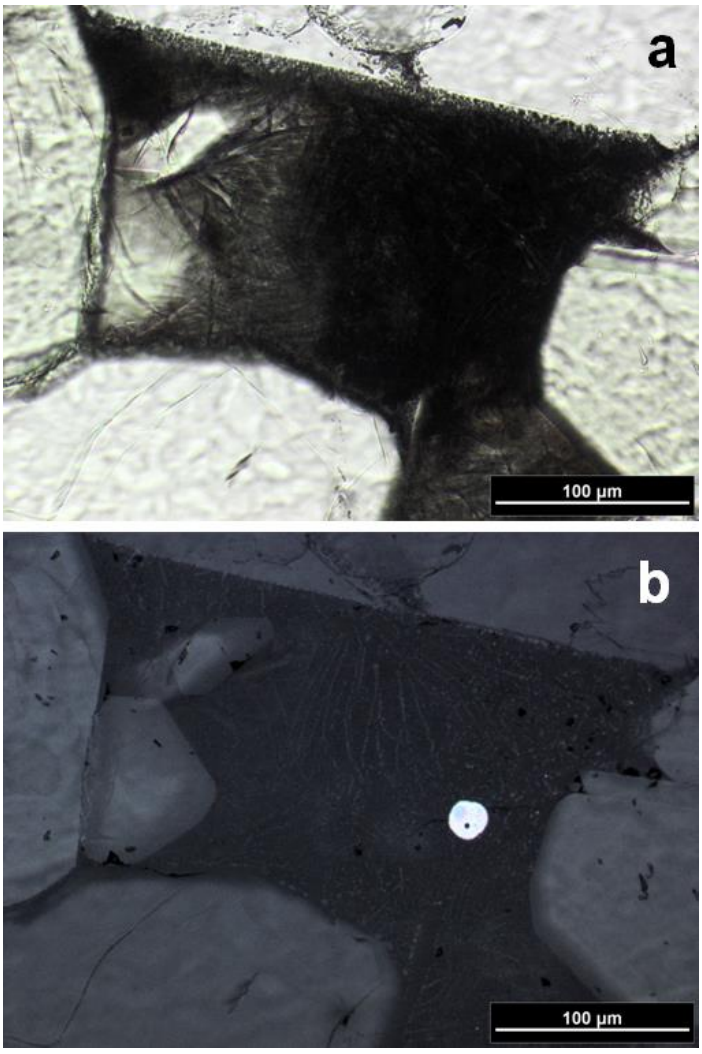

Fig. S3. Glassy melt inclusion in ALM-A demonstrating the rapid cooling of the lava. (a) interstitial melt having small skeletal crystallites; transmitted polarized light; (b) tiny skeletal crystals and a metal-sulfide spherule embedded in a glassy groundmass; reflected light.

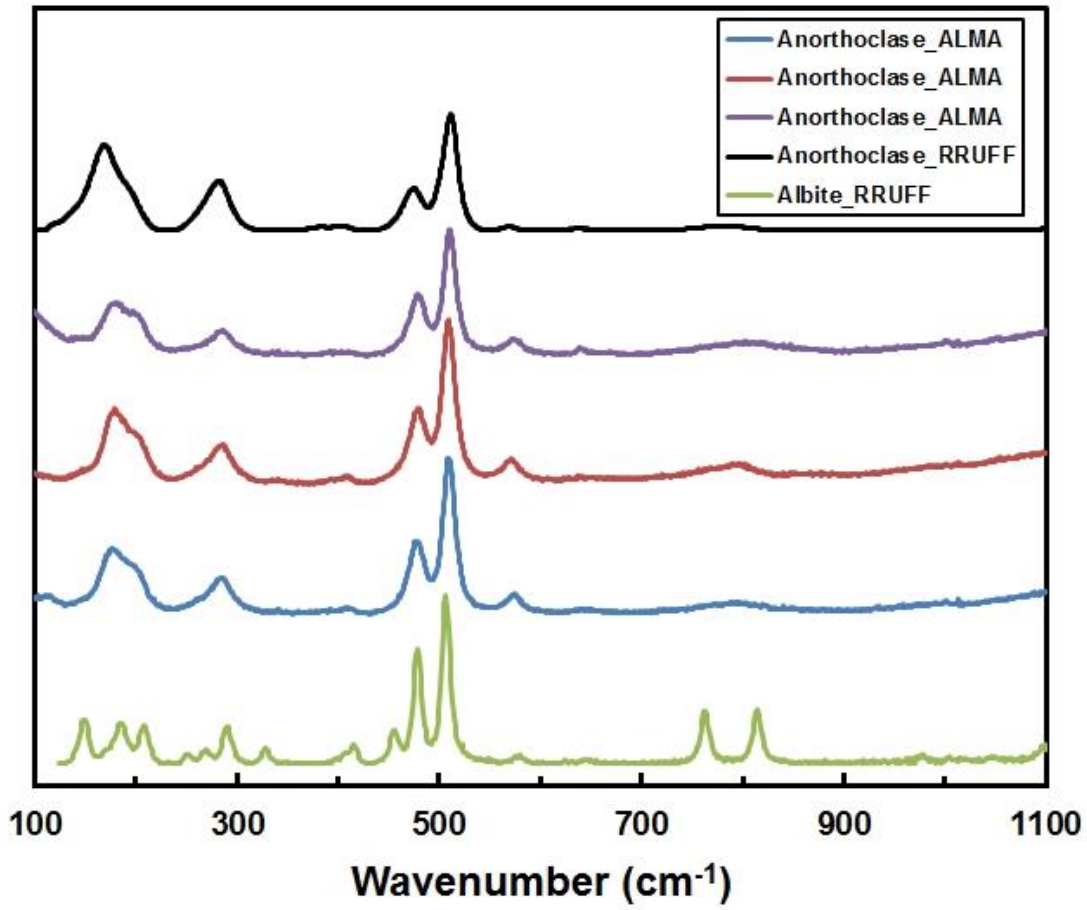

Fig. S4. Raman spectra of anorthoclase grains from ALM-A compared to spectra from the RRUFF database (1) of albite and anorthoclase. Spectra of ALM-A grains can be clearly identified as anorthoclase. The slight shift of band A around 170 cm^{-1} compared to the reference can be related to a chemical effect due to different K and Na contents (2).

1. Downs RT (2006) The RRUFF Project: an integrated study of the chemistry, crystallography, Raman and infrared spectroscopy of minerals. Program and Abstracts of the 19th *General Meeting of the International Mineralogical Association* in Kobe, Japan. O03-13.

2. Bendel V, Schmidt BC (2008) Raman spectroscopic characterisation of disordered alkali feldspars along the join $KAlSi_3O_8$–$NaAlSi_3O_8$: application to natural sanidine and anorthoclase. *Eur J Min* 20:1055-1065.

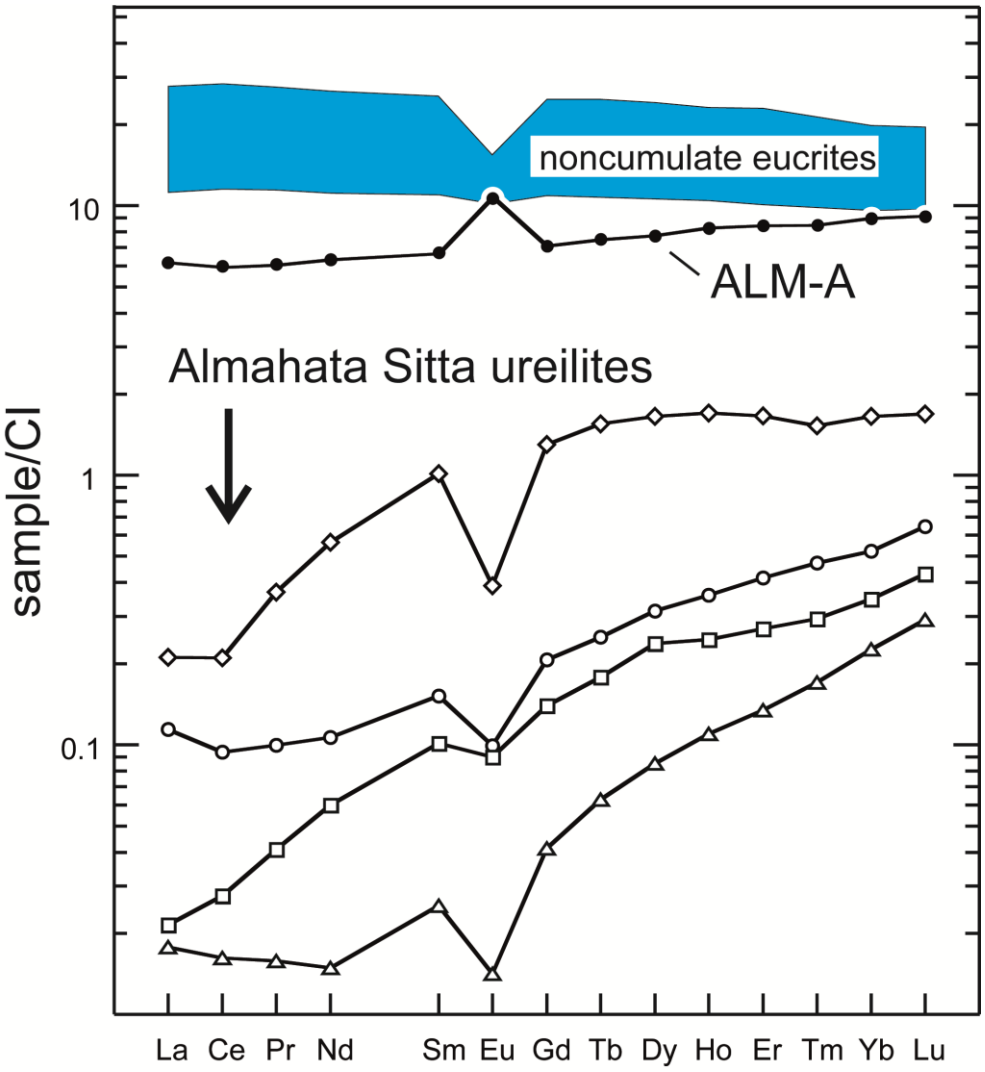

Fig. S5. REE patterns of ALM-A and Almahata Sitta ureilites (1). Noncumulate eucrites are shown for comparison (2). The reference for CI chondrites is from (3).

1. Friedrich JM, et al. (2010) The elemental composition of Almahata Sitta. *Meteorit Planet Sci* 45:1718-1727.

2. Barrat JA, et al. (2007) The Stannern trend eucrites: Contamination of main group eucritic magmas by crustal partial melts. *Geochim Cosmochim Acta* 71:4108-4124.

3. Barrat JA, et al. (2012) Geochemistry of CI chondrites: Major and trace elements, and Cu and Zn Isotopes. *Geochim Cosmochim Acta* 83:79-92.

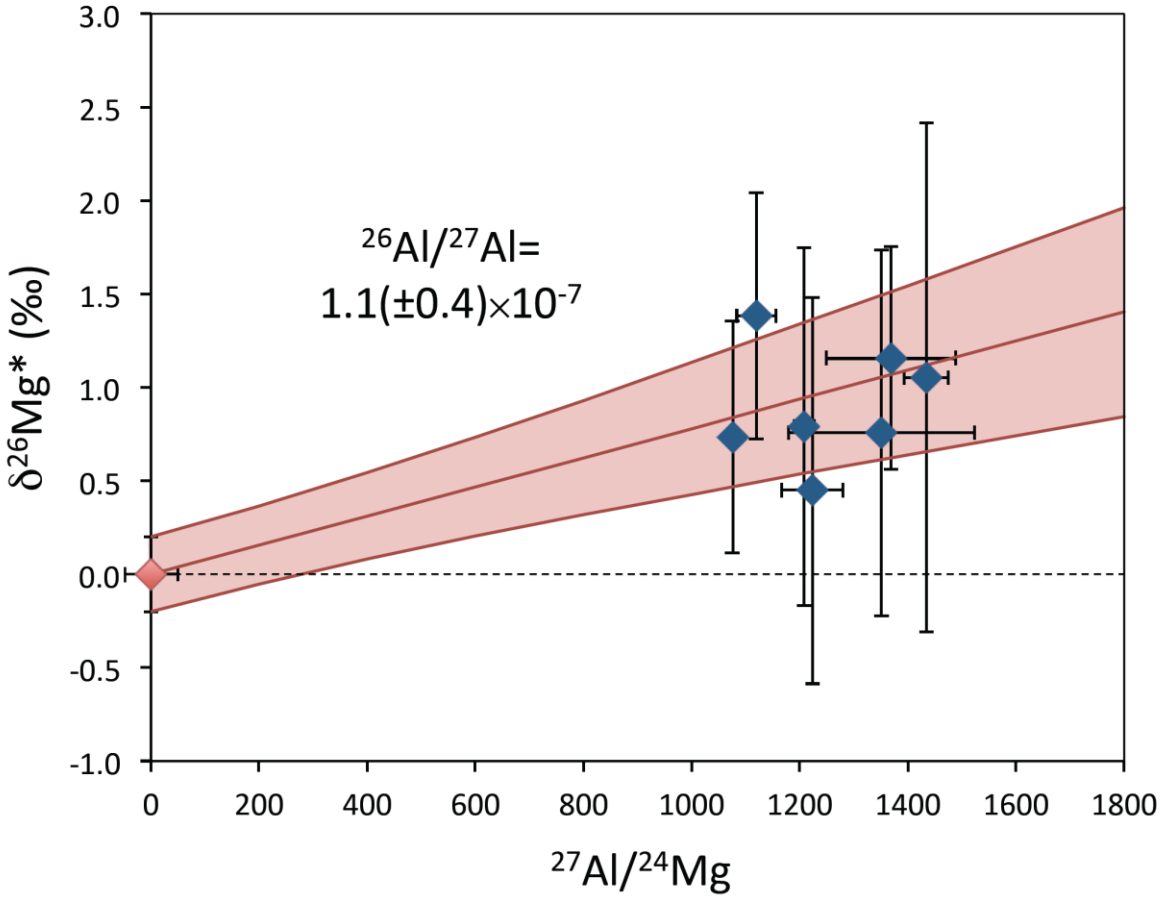

Fig. S6. ^{26}Al isochron for ALM-A. Data for 7 feldspar grains from ALM-A are shown as blue diamonds with two sigma errors for the ^{26}Mg excesses (given in delta unit in permil as δ^{26}Mg* on the Y axis) and the ^{27}Al/^{24}Mg atomic ratios on the X axis. The regression line has been calculated assuming an intercept of δ^{26}Mg*=0±0.2‰ (red diamond). This gives a slope of 7.8±(2.9)×10^{-4} (error envelope shown in red) corresponding to a ^{26}Al/^{27}Al ratio of 1.1(±0.4)×10^{-7}.

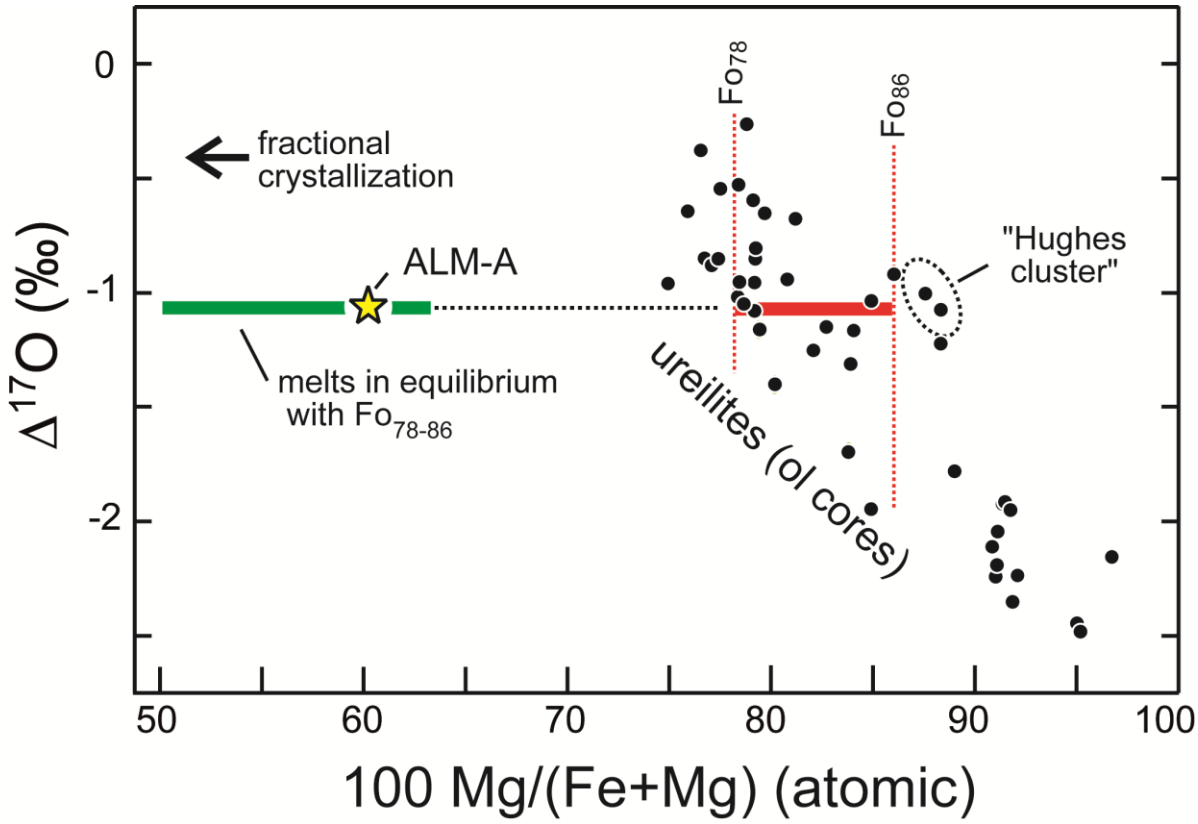

Fig. S7. $\Delta^{17}O$ vs. Mg# for ALM-A and ureilites. $\Delta^{17}O$ data and olivine core compositions taken from Clayton and Mayeda (1) and Downes et al. (2), respectively. Hughes type ureilites are unusual augite-bearing rocks petrologically distinct from the other ureilites (3).

1. Clayton RN and Mayeda TK (1996) Oxygen isotope studies of achondrites. *Geochim Cosmochim Acta* 60:1999-2017.

2. Downes H, Mittlefehldt DW, Kita NT, Valley JW (2008) Evidence from polymict ureilite meteorites for a disrupted and re-accreted single ureilite parent asteroid gardened by several distinct impactors. *Geochim Cosmochim Acta* 72:4825-4844.

3. Goodrich CA, Fioretti AM, Van Orman JA (2009) Petrogenesis of augite-bearing ureilites Hughes 009 and FRO 90054/93008 inferred from melt inclusions. *Geochim Cosmochim Acta* 73:3055-3076.

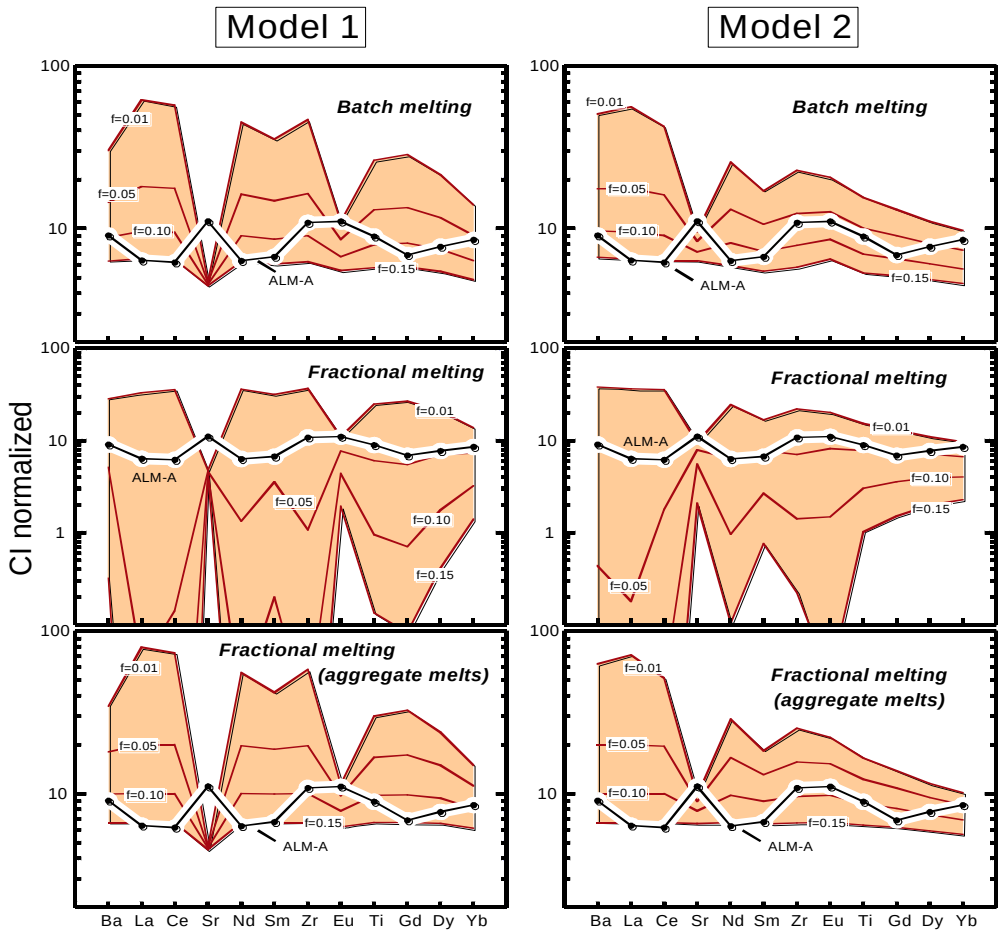

Fig. S8. Trace element abundances of melts generated from a source with CI abundances. The models include (a) the classical batch partial melting (equilibrium), (b) fractional melting ("instantaneous" melts), and (c) the aggregate melts formed from fractional melting. Data for ALM-A are given for comparison. Two mineralogical assemblages were tested. The model 1 corresponds to an olivine-pigeonite-augite-plagioclase using the modal and melting proportions given by (1). The model 2 corresponds to an olivine-augite-plagioclase assemblage using the modal proportions and the melting proportions given by (2). The partition coefficients are the same as those literature data given for Zr (3) and the other elements (4). None of the models reproduces satisfactorily the trace element abundances of ALM-A.

1. Warren PH; Kallemeyn GW (1992) Explosive volcanism and the graphite oxygen fugacity buffer on the parent asteroid(s) of the ureilite meteorites. *Icarus* 100:110-126.

2. Goodrich CA, Van Orman J, Wilson L (2007). Fractional melting and smelting on the ureilite parent body. *Geochim Cosmochim Acta* 71:2876-2895.

3. Münker C. (2010) A high field strength element perspective on early lunar differentiation. *Geochim Cosmochim Acta* 74:7340-7361.

4. Warren PH (2008) A depleted, not ideally chondritic bulk Earth: The explosive-volcanic basalt loss hypothesis. *Geochim Cosmochim Acta* 72:2217-2235.

Table S1. Composition of feldspar ordered by increasing An-contents.

	SiO_2	Al_2O_3	FeO	CaO	Na_2O	K_2O	Total	An	Ab	Or
Feldspar	66.5	20.0	0.07	1.84	10.5	0.60	99.51	8.5	88.2	3.3
	66.4	19.9	0.09	1.99	10.4	0.48	99.26	9.3	88.0	2.7
	66.5	20.1	0.05	2.15	10.4	0.56	99.76	10.0	87.0	3.1
	66.0	20.6	0.32	2.35	10.3	0.44	100.01	11.0	86.6	2.5
	65.7	20.7	0.17	2.77	10.2	0.46	100.00	12.7	84.7	2.5
	65.2	20.9	0.09	3.2	10.0	0.39	99.78	14.5	83.4	2.1
	64.7	21.2	0.05	3.4	9.6	0.45	99.40	15.8	81.7	2.5
	64.4	21.3	0.17	3.5	9.5	0.38	99.25	16.5	81.3	2.1
	64.1	21.8	<0.02	3.8	9.4	0.36	99.48	17.7	80.2	2.0
	63.6	21.8	0.05	4.0	9.7	0.31	99.46	18.2	80.1	1.7
	63.1	22.3	0.10	4.5	9.3	0.31	99.61	20.8	77.5	1.7
	63.3	22.6	<0.01	4.5	9.1	0.35	99.86	21.1	76.9	2.0
	62.3	23.0	0.09	5.0	9.0	0.23	99.62	23.1	75.6	1.3
	61.5	23.4	0.06	5.4	9.1	0.22	99.68	24.4	74.4	1.2
	61.3	23.8	0.07	5.7	8.7	0.23	99.80	26.4	72.4	1.3
	61.1	23.8	0.08	6.0	8.3	0.26	99.54	27.9	70.7	1.4
	60.8	23.6	0.11	6.3	8.2	0.21	99.22	29.3	69.5	1.2
	60.6	24.1	0.19	6.4	8.0	0.20	99.49	30.5	68.4	1.1
	60.5	24.2	0.06	6.5	7.7	0.20	99.16	31.4	67.5	1.1
	59.4	24.7	0.67	7.1	7.6	0.18	99.65	33.8	65.2	1.0
	58.6	25.0	0.08	7.7	7.6	0.14	99.12	35.6	63.6	0.8
	58.9	25.5	<0.01	8.0	7.2	0.16	99.77	37.7	61.4	0.9
	58.0	25.8	<0.04	8.2	6.8	0.13	98.97	39.8	59.4	0.8
	58.0	25.8	0.10	8.6	6.7	0.12	99.32	41.1	58.2	0.7
	57.4	26.0	0.07	8.9	6.5	0.17	99.04	42.6	56.4	1.0
	57.0	26.4	0.06	9.2	6.7	0.14	99.50	42.8	56.4	0.8
	57.8	26.4	0.06	9.2	6.3	0.13	99.89	44.2	55.1	0.8
	56.8	26.9	0.07	9.6	6.4	0.10	99.87	45.1	54.3	0.5
	56.8	26.8	0.07	9.8	6.1	0.14	99.71	46.6	52.6	0.8
	56.7	27.1	0.09	9.9	6.0	0.12	99.91	47.5	51.8	0.7
	56.1	27.0	<0.01	10.1	5.9	0.09	99.20	48.4	51.1	0.5
	55.7	27.6	<0.03	10.7	5.9	0.09	100.02	49.8	49.7	0.5
	55.4	27.3	<0.04	10.5	5.7	0.11	99.05	50.0	49.4	0.6
	55.4	27.3	0.07	10.3	5.6	0.11	98.78	50.0	49.3	0.6
	54.9	27.8	0.11	10.8	5.7	0.10	99.41	51.0	48.5	0.5
	55.1	27.7	<0.03	11.1	5.5	0.10	99.53	52.5	46.9	0.5
	54.8	27.5	<0.01	11.0	5.3	0.06	98.67	53.0	46.7	0.3

Data in wt%; < = Value is below detection limit. An-, Ab-, and Or-contents in mol%.

Table S2. Chemical composition of Ca-rich and low-Ca pyroxene, spinels, ilmenite, and the SiO_2-rich glassy component.

	SiO_2	TiO_2	Al_2O_3	Cr_2O_3	FeO	MnO	MgO	CaO	Na_2O	K_2O	Total	En	Fs	Wo
Ca-rich pyroxene	51.8	1.31	0.57	0.90	12.0	0.76	14.7	16.9	0.72	<0.02	99.68	43.7	20.1	36.2
	51.9	1.35	0.55	0.88	11.8	0.69	14.5	17.4	0.71	<0.01	99.79	43.1	19.8	37.1
	52.2	1.25	0.52	0.83	12.0	0.75	14.3	17.4	0.70	n.d.	99.95	42.7	20.0	37.3
	52.1	1.28	0.53	0.89	11.9	0.79	14.3	17.5	0.69	<0.02	100.00	42.6	20.0	37.4
	52.3	1.26	0.53	0.91	11.7	0.76	14.4	17.4	0.67	0.04	99.97	42.9	19.7	37.5
	52.0	1.31	0.53	0.91	11.7	0.73	14.4	17.5	0.72	n.d.	99.80	42.8	19.6	37.5
	52.0	1.24	0.53	0.85	11.9	0.79	14.4	17.7	0.65	n.d.	100.06	42.6	19.8	37.6
	52.1	1.33	0.51	0.89	11.6	0.75	14.4	17.6	0.64	n.d.	99.82	42.9	19.5	37.7
	52.0	1.35	0.52	0.91	11.8	0.72	14.2	17.7	0.79	<0.01	100.00	42.4	19.7	37.8
	52.0	1.28	0.50	0.90	11.9	0.71	14.2	17.7	0.62	<0.03	99.84	42.3	19.8	37.9
	51.8	1.31	0.56	0.89	11.8	0.81	14.2	17.7	0.71	n.d.	99.78	42.3	19.7	38.0
	52.0	1.32	0.54	0.92	11.7	0.76	14.3	17.8	0.70	n.d.	100.04	42.5	19.5	38.0
	52.3	1.29	0.52	0.89	11.6	0.73	14.3	17.7	0.72	<0.01	100.06	42.6	19.4	38.1
	SiO_2	TiO_2	Al_2O_3	Cr_2O_3	FeO	MnO	MgO	CaO	Na_2O	K_2O	Total	En	Fs	Wo
low Ca-pyroxene	52.2	0.62	0.28	0.37	21.6	1.26	19.7	3.9	0.19	n.d.	100.12	56.9	35.0	8.1
	52.4	0.57	0.21	0.37	21.7	1.21	19.4	3.9	0.18	n.d.	99.94	56.5	35.4	8.1
	52.1	0.55	0.23	0.40	22.0	1.20	19.5	4.0	0.20	n.d.	100.18	56.2	35.6	8.2
	52.3	0.58	0.21	0.37	21.8	1.25	19.3	4.0	0.16	n.d.	99.97	56.2	35.5	8.3
	52.2	0.57	0.22	0.39	21.8	1.25	19.4	4.0	0.18	n.d.	100.01	56.3	35.4	8.3
	52.3	0.60	0.24	0.43	21.5	1.18	19.5	4.1	0.22	n.d.	100.07	56.6	35.0	8.5
	52.1	0.59	0.23	0.40	21.7	1.24	19.4	4.1	0.16	n.d.	99.92	56.2	35.3	8.5
	52.4	0.53	0.22	0.42	21.7	1.23	19.6	4.1	0.20	<0.02	100.42	56.4	35.0	8.6
	52.2	0.71	0.30	0.47	19.9	1.19	18.5	6.4	0.33	<0.01	100.01	53.9	32.6	13.5
	SiO_2	TiO_2	Al_2O_3	Cr_2O_3	FeO	MnO	MgO	CaO	Na_2O	K_2O	Total			
Spinel	0.09	19.8	2.48	29.2	41.1	1.05	4.4	0.10	0.08	n.d.	98.30			
	0.06	19.7	2.49	29.0	42.5	1.00	3.7	0.05	0.03	n.d.	98.53			
	0.08	20.1	2.07	28.7	41.9	1.04	4.3	0.30	0.12	n.d.	98.61			
	0.05	20.1	2.33	29.2	41.9	1.04	4.3	0.08	0.04	n.d.	99.04			
	0.05	20.0	2.45	29.1	42.4	1.02	3.8	0.14	0.08	n.d.	99.04			
	0.07	19.8	2.21	28.8	43.5	1.05	3.4	0.13	0.11	<0.01	99.08			
	0.05	20.3	2.08	29.8	42.2	1.07	3.9	0.06	0.07	n.d.	99.53			
	0.04	20.8	1.96	30.0	41.8	1.10	4.0	<0.01	0.03	n.d.	99.74			
	0.04	20.8	2.19	29.6	41.8	1.09	4.1	0.08	0.06	n.d.	99.76			
	0.04	20.6	2.15	29.8	42.0	1.05	4.2	0.03	0.03	n.d.	99.90			
	SiO_2	TiO_2	Al_2O_3	Cr_2O_3	FeO	MnO	MgO	CaO	Na_2O	K_2O	Total			
Ilmenite	n.d.	52.7	0.07	1.45	38.3	1.07	5.0	0.28	<0.01	n.d.	98.88			
	<0.01	53.3	0.12	1.82	38.1	1.13	5.3	0.12	n.d.	n.d.	99.90			
	<0.01	53.8	0.06	1.84	38.3	1.18	5.1	<0.02	0.03	<0.02	100.36			
	<0.02	54.6	0.07	2.05	37.3	1.16	5.2	0.05	n.d.	n.d.	100.45			
	n.d.	54.1	0.08	1.87	37.4	1.13	5.7	0.14	0.07	n.d.	100.49			
	<0.02	54.1	0.05	1.72	38.2	1.16	5.4	<0.02	<0.01	n.d.	100.68			
	<0.02	54.6	0.09	2.14	37.4	1.11	5.3	<0.02	0.08	n.d.	100.76			
	<0.01	53.9	0.09	1.98	38.0	1.07	5.7	<0.02	<0.01	<0.02	100.80			
	0.04	55.2	0.09	2.35	37.0	1.12	5.0	n.d.	n.d.	n.d.	100.80			
	<0.02	53.9	0.07	1.98	38.3	1.17	5.4	0.03	0.07	n.d.	100.94			
	SiO_2	TiO_2	Al_2O_3	Cr_2O_3	FeO	MnO	MgO	CaO	Na_2O	K_2O	Total			
SiO_2-rich glass	73.4	1.73	13.6	<0.02	3.5	0.12	0.20	0.54	3.8	1.68	98.59			
	71.4	1.77	13.1	<0.02	3.9	0.14	0.20	0.56	4.6	3.4	99.09			
	72.3	1.87	13.4	<0.02	4.2	0.12	0.20	0.72	4.6	1.98	99.41			
	74.0	1.61	13.9	<0.05	3.4	0.12	0.10	0.52	4.2	1.59	99.49			
	72.0	1.72	13.6	<0.03	3.2	0.08	0.20	0.47	4.2	4.0	99.50			
	72.5	1.68	13.4	<0.02	3.2	0.08	0.20	0.52	4.2	4.3	100.10			
	72.7	2.04	13.8	<0.02	3.7	0.12	0.20	0.62	4.2	2.78	100.18			
	72.5	1.84	13.5	<0.03	3.1	0.12	0.20	0.56	4.2	4.1	100.15			

Data in wt%; n. d. = not detected, < = value is below detection limit. En-, Fs-, and Wo-contents in mol%; the SiO_2-rich glass contains about 0.5-0.7 wt% P_2O_5.

Table S3. Chemical composition of Cl-apatite

	P1-1	P3-1	P3-2	P2-1	P2-2	P2-3	P4-1	P4-2	P5-1	P7-1
CaO	52.8	52.6	52.1	51.4	52.2	52.2	51.9	52.6	52.2	52.2
P_2O_5	41.2	41.3	40.7	41.1	41.0	40.7	41.0	41.0	41.0	41.4
FeO	0.77	0.83	0.87	0.80	0.83	0.67	0.68	0.61	0.69	0.74
MgO	0.44	0.47	0.49	0.51	0.44	0.42	0.45	0.47	0.45	0.43
MnO	0.19	0.18	0.15	0.20	0.21	0.20	0.15	0.13	0.19	0.21
SrO	0.14	0.14	0.16	0.09	0.14	0.13	< 0.03	0.16	0.13	0.08
Na_2O	0.62	0.62	0.54	0.63	0.62	0.61	0.63	0.63	0.55	0.56
K_2O	< 0.02	0.05	0.08	n.d.	n.d.	n.d.	n.d.	< 0.03	< 0.02	< 0.02
SiO_2	0.23	0.23	0.36	0.26	0.24	0.21	0.29	0.28	0.28	0.29
TiO_2	n.d.	n.d.	< 0.02	n.d.	n.d.	n.d.	0.04	n.d.	0.07	n.d.
Al_2O_3	n.d.	0.04	< 0.02	n.d.	n.d.	n.d.	n.d.	n.d.	< 0.02	< 0.02
Cr_2O_3	< 0.03	n.d.	n.d.	< 0.02	0.04	< 0.03	0.04	n.d.	n.d.	< 0.02
SO_3	0.04	< 0.03	0.04	0.04	0.04	0.04	0.04	< 0.03	0.06	n.d.
Cl	3.1	2.9	2.9	3.1	3.0	3.1	2.8	3.1	3.2	3.1
F	1.57	1.32	1.39	1.37	1.46	1.32	1.51	1.56	1.40	1.43
H_2O	0.21	0.38	0.33	0.30	0.27	0.31	0.30	0.22	0.27	0.28
total	**101.36**	**101.09**	**100.15**	**99.82**	**100.49**	**99.94**	**99.86**	**100.82**	**100.53**	**100.78**

Stoichiometric calculations (based on 26 oxygens)

	P1-1	P3-1	P3-2	P2-1	P2-2	P2-3	P4-1	P4-2	P5-1	P7-1
Ca	9.694	9.699	9.690	9.571	9.673	9.736	9.638	9.708	9.666	9.615
P	5.984	6.014	5.984	6.040	5.998	5.998	6.022	5.983	5.998	6.035
Fe	0.110	0.119	0.127	0.117	0.119	0.098	0.098	0.088	0.100	0.106
Mg	0.113	0.121	0.126	0.132	0.114	0.109	0.117	0.120	0.116	0.111
Mn	0.028	0.026	0.022	0.030	0.031	0.030	0.022	0.019	0.028	0.030
Sr	0.014	0.014	0.016	-	0.014	0.013	-	0.016	0.013	-
Na	0.205	0.205	0.181	0.211	0.208	0.206	0.213	0.211	0.183	0.188
K	-	-	0.018	-	-	-	-	-	-	-
Si	0.040	0.040	0.062	0.044	0.041	0.037	0.050	0.048	0.048	0.050
Ti	-	-	-	-	-	-	-	-	-	-
Al	-	-	-	-	-	-	-	-	-	-
Cr	-	-	-	-	-	-	-	-	-	-
S	-	-	-	-	-	-	-	-	-	-
Cl	0.904	0.842	0.857	0.904	0.887	0.916	0.827	0.897	0.929	0.895
F	0.854	0.719	0.761	0.751	0.797	0.726	0.825	0.849	0.763	0.779
OH	0.243	0.439	0.383	0.345	0.315	0.358	0.348	0.254	0.308	0.326
total	18.189	18.248	18.227	18.145	18.197	18.227	18.160	18.193	18.152	18.135
cations	**16.188**	**16.248**	**16.226**	**16.145**	**16.198**	**16.227**	**16.160**	**16.193**	**16.152**	**16.135**
(OH)+F+Cl	2.00	2.00	2.00	2.00	2.00	2.00	2.00	2.00	2.00	2.00
X_{Cl}	0.45	0.42	0.43	0.45	0.44	0.46	0.41	0.45	0.46	0.45
X_F	0.43	0.36	0.38	0.38	0.40	0.36	0.41	0.42	0.38	0.39
X_{OH}	0.12	0.22	0.19	0.17	0.16	0.18	0.17	0.13	0.15	0.16

Data in wt%; H_2O-concentrations calculated; n. d. = not detected, < = value is below detection limit.

Table S4. Results on Al-Mg isotope analyses of 7 feldspar grains from ALM-A.

Sample #	$^{27}Al/^{24}Mg$	2σ $^{27}Al/^{24}Mg$	$\Delta^{26}Mg$	2σ $\Delta^{26}Mg$
A4	1433.9	40.9	1.1	1.4
A3	1351.4	172.1	0.8	1.0
A2	1119.6	36.4	1.4	0.7
A1	1208.3	18.9	0.8	1.0
A5	1369.0	119.3	1.2	0.6
A6	1223.5	56.1	0.4	1.0
B1b-1	1075.7	8.8	0.7	0.6